# Magnetic Reconnection Between Colliding Magnetized, Laser-Produced Plasma Plumes

Throughout the universe, magnetic reconnection makes it possible for the magnetic field to change its topology and thereby allow an explosive release of stored energy.[1–3] Some vivid examples of magnetic reconnection are solar flares,[4] sawtooth crashes and relaxation processes in tokamaks and reversed-field pinches,[5,6] and magnetospheric substorms.[4,7] Magnetic reconnection in high-energy-density (HED) plasma is of great interest because of the indication of the major role it plays in astrophysical phenomena such as accretion disks and stellar flares.[8–10] The laboratory-based experimental study of magnetic reconnection in HED plasma is a relatively recent development. These experiments studied the reconnection of the self-generated (e.g., Biermann battery) magnetic fields between colliding laser-produced plasma plumes.[11–15] Magnetic-field destruction[12] has been observed, as well as plasma jets[11,13–15] and electron energization.[15]

This article presents, for the first time, results of the reconnection of an externally applied magnetic field by counter-propagating, colliding HED plasmas. These experiments are based on new techniques that externally control the magnetization of ablated plasma plumes. This allows one to directly compare experiments with and without an external magnetic field. The results obtained here are completely different from recent experiments with zero external magnetic fields that are dominated by the collisionless interpenetration of two plasma streams and the generation of Weibel instability.[16] The geometry of this externally magnetized plasma experiment makes it amenable to end-to-end simulation with particle-in-cell codes modeling the entire progression of the experiment, including plasma formation and the assembly of the current sheet. While previous results in HED plasmas could infer reconnection through destruction of the magnetic field,[12] this work is the first to observe clear stagnation of the counter-propagating magnetized ribbons and the formation of an extended current sheet. The current sheet stagnates at a width comparable to the ion skin depth and shows the formation of cellular structures that may indicate the formation of magnetic islands or plasmoids. Finally, the magnetic fields in the current sheet are observed to suddenly and completely annihilate, an effect not yet captured in our two-dimensional (2-D) simulation.

The experiment was carried out on LLE's OMEGA EP Laser System.[17] Figure 139.1 shows the experimental setup. Two counter-propagating plasma plumes were obtained by irradiating oppositely placed plastic (CH), $2 \times 6 \times 0.25$-mm$^3$ ablator targets with two 1.8-kJ, 2-ns laser beams (drive beams) at a wavelength of 0.351 $\mu$m and on-target laser intensities of $5 \times 10^{13}$ W/cm$^2$. The targets were separated by the width $2L$ = 4.25 mm and the laser beam's incidence angle was $\theta = 74°$, resulting in highly elliptical, $1 \times 3$-mm$^2$ focal spots. The highly elongated focal footprint shape conforms to a quasi-2-D geometry, making it suitable for comparison with 2-D simulations.

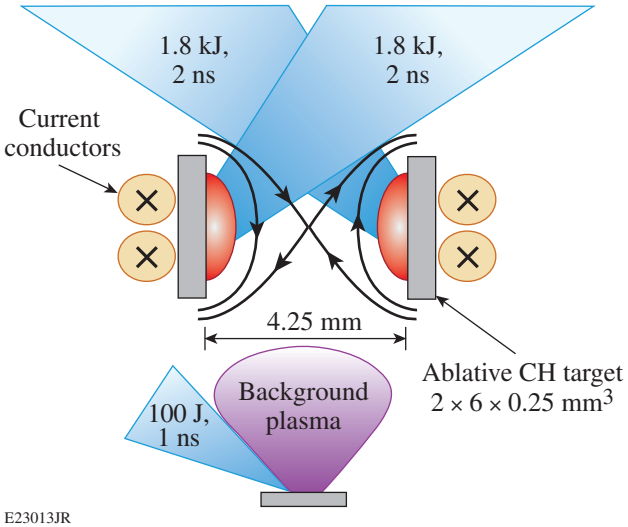


Figure 139.1
Experimental setup. Two counter-propagating plasma plumes were obtained by irradiating with two laser beams opposing plastic (CH) ablator targets. An external magnetic field was created by pulsing an electric current through conductors located directly behind each target. The region between the ablator targets was prefilled by a tenuous background plasma created by a dedicated laser–ablator pair. A multi-MeV proton beam (not shown) generated with a high-intensity, short-pulse laser beam was used to probe the dynamics and topology of the magnetic field in the interaction region.

An external magnetic field, imposed perpendicular to the plasma flow, was created by current-carrying conductors placed directly behind each target and powered by MIFEDS (magneto-inertial fusion electrical discharge system).[18] The current pulse had a duration of 1 $\mu$s and the drive lasers were fired at the peak of the magnetic field. Two parallel currents (see Fig. 139.1) were used to impose a field with an x-type null point (x point) and field reversal between the colliding plasmas—a typical reconnection geometry.[1,3] The magnetic-field strength $B$ was monotonically increased from $B = 0$ at the midplane to $B = 8$ T at the targets. The vacuum magnetic flux ($\int B_z dx$ from the foil to the x point) available for reconnection is $\sim 8 \times 10^{-3}$ Tm. In the process of the plumes colliding and merging, the magnetic field is expected to be first compressed into a current sheet, accompanied by reconnection.

The x-point region between the ablators was prefilled by a tenuous background plasma created by ablating a third target ($2 \times 2 \times 0.25$ mm$^3$ and 7 mm from the x point) with a third laser pulse (100 J, 1 ns), fired 12 ns prior to the main drive beams to give the plume enough time to prefill the interaction volume. These laser and target parameters were chosen experimentally to obtain desirable background plasma parameters at the moment when the drive beams fired. The background plasma facilitates the reconnection by allowing the current through the x-point region. Experiments without a background plasma showed no reconnection.

The dynamics and topology of the magnetic field in the interaction region were probed with proton radiography.[19] This diagnostic used an ultrafast proton beam generated with a high-intensity, short-pulse laser beam (1.053 $\mu$m/800 J/10 ps) focused to a 25-$\mu$m spot on a thin 20-$\mu$m copper foil. The protons, accelerated by the target-normal sheath acceleration (TNSA) mechanism,[20] have a broad distribution of energies of the order of 10 MeV and higher. Protons are detected in a stack of radiochromic film (RCF) interleaved with aluminum foils of various thicknesses. The RCF detector is placed 80 mm from the interaction region, for a geometrical magnification of $M = 11$, with proton energies resolved in the film stack by their respective energy-dependent Bragg peaks. The temporal resolution of the detector is ~100 ps. While passing through the interaction region (Fig. 139.1), the protons are focused or defocused by magnetic fields in the magnetized plumes, leaving an intensity pattern at the detector. The temporal evolution of the magnetic-field structure was obtained over multiple shots by varying the timing of the proton beam with respect to the drive-laser beams.

A series of representative proton radiography images in Figs. 139.2(a)–139.2(d) illustrate four stages in the magnetic-field evolution: (a) the formation of magnetic "ribbons" and the sweeping up of background plasma and magnetic field, (b) the collision of magnetic ribbons, (c) reconnection, and (d) magnetic-field annihilation. The time stamps on each frame show the time when the proton beam fired relative to the drive beams. Distinctive features common to all the images are the two light-colored curved bands containing a high magnetic field, described here as "magnetic ribbons." The direction of the vertical component of the magnetic field, upward on the right ribbon and downward on the left ribbon (see Fig. 139.1), is such that the diagnostic protons are deflected outward from each corresponding ribbon. The magnetic field in the ribbons is strong enough to completely deflect the protons from those regions, leaving a deficit of protons and reflected as white, unexposed film. A sharp, "caustic" proton boundary[21] of very high fluence—a feature well-reproduced in our modeling—appears immediately on the outside of each ribbon, forming an important point of comparison between simulation and experiment.

During the plume expansion stage [Fig. 139.2(a)], the shape of the ribbons is topologically equivalent to the shape of the vacuum magnetic-field lines (Fig. 139.1). At $t = 2.37$ ns, each ribbon has traversed more than halfway to the midplane. The magnetic field in each ribbon has been strongly compressed above the vacuum field, as indicated by a low proton fluence in the ribbons. This stage is a clear manifestation of the initial magnetic field being swept up by the high-pressure plasma plumes, as would be expected by the high plasma pressure compared to the magnetic-field pressure. The degree of field compression by the pileup can be estimated by assuming that all of the initially available flux $\Phi \approx 8$ T mm is compressed into a ribbon with a thickness of $\delta \approx 0.3$ mm, resulting in a compressed field $B_{\text{comp}} \approx \Phi/\theta \approx 25$ T.

At $t = 3.12$ ns [Fig. 139.2(b)], the ribbons collide and flatten out. The magnetic field in the collision region is strongly compressed, expelling virtually all the fast protons. The ribbon width stagnates, indicating stagnation of the plasma flow. Based on the opposing signs of the incoming magnetic fields, the collision of the ribbons must produce a reconnecting current sheet.

Figure 139.2(c) shows the magnetic field at a late nonlinear phase of reconnection, demonstrating a clear evolution in the topology of the current sheet. The plasma elements that were previously connected by the magnetic field (e.g., B and C) are now disconnected. Conversely, plasma elements that were pre-

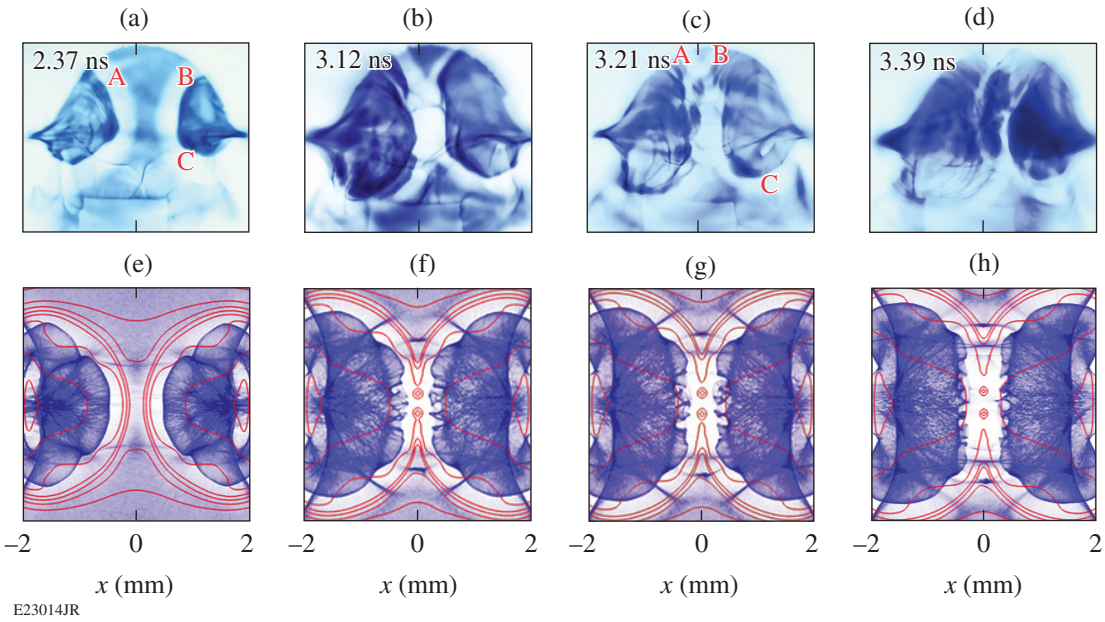


Figure 139.2
Proton radiographic images of the magnetic-field evolution. The ablator targets are situated at the left and right borders of each frame. Dark areas correspond to high proton fluence. The series illustrates four stages in the magnetic-field evolution: (a) formation of magnetic "ribbons" and the sweeping up of background plasma and magnetic field, (b) collision of magnetic ribbons, (c) reconnection, and (d) magnetic-field annihilation. The time stamps on each frame show the time when the proton beam fired relative to the drive beams. The horizontal and vertical scales are the same. [(e)–(h)] Results of simulated proton radiography at the corresponding times are shown in blue, with overlaid magnetic-field lines (red curves).

viously disconnected (e.g., A and B) are now connected by the newly formed outflow magnetic field (V-shaped ribbons at the top and bottom parts of the merged area) that disconnects from the central part of the current sheath and starts moving away. Furthermore, a small number of cellular structures appear, spanning the width of the current sheet. These structures can be plausibly interpreted as magnetic islands or plasmoid structures growing inside the current sheet.

Finally, Fig. 139.2(d) shows the beginning of the disruption of the current sheet and complete annihilation of the magnetic fields, as the protons are no longer defocused from the sheet. The onset of this process may be reflected in the two dark areas at the top of the current sheet in Fig. 139.2(c). The annihilation (and indeed the entire evolution of the ribbons) occurs on a significantly faster time scale than the resistive diffusion (~10 ns) through the smallest plasma structures (~100 $\mu$m), so neither the reconnection nor disruption is due simply to resistive dissipation. (Here, the magnetic-diffusion coefficient $D_m = \eta/\mu_0$ was evaluated from the Spitzer resistivity $\eta$ at $T_e$ = 200 eV, a baseline prediction from simulations with the radiation–hydrodynamics code *DRACO*[22] and likely an underestimate of the temperature.)

Figures 139.2(e)–139.2(h) show results of accompanying particle-in-cell (PIC) simulations, which agree with the experiment on a number of features of the colliding ribbons. The 2-D simulations, with the invariant direction parallel to the MIFEDS currents, were conducted with the code *PSC*[23,24] to help with both design and analysis of the experiments. The code solves the full relativistic, electromagnetic Vlasov–Maxwell system and includes a collision operator implementing Fokker–Planck collisions.[24] The PIC model has long been used to simulate magnetic reconnection;[23,24] in particular, it retains kinetic effects of the electrons in the current sheet, allowing for collisionless reconnection. The simulations provide an end-to-end model of the experiments, starting from the vacuum magnetic field and followed by plasma formation, which is modeled with particle source terms set to obtain profiles similar to that provided by *DRACO*.[22] *DRACO* predicts plasma ablation densities near $6 \times 10^{26}$ m$^{-3}$ and background plasma densities near $2 \times 10^{24}$ m$^{-3}$. Time is calibrated between simulation and experiment by matching the location of the ribbons at 2.37 ns; this corresponds to a sound speed of $1.8 \times 10^5$ m/s, which is, in fact, quite close to nominal *DRACO* predictions of $2 \times 10^5$ m/s. The magnetic fields were initialized as the vacuum fields from the two

conductors. More-detailed results of these simulations will be reported separately.

Synthetic proton radiographic images are obtained using a proton ray-tracing model. Protons are initialized from a point source and projected through the simulation domain, where they receive an impulse by the line-integrated $v \times B$ force, and are finally projected to the detector. The line integration, since it is along the invariant direction of the simulations, is accounted for by simply multiplying by a characteristic length, taken as 4 mm. The final proton locations are binned to form a fluence image. In Figs. 139.2(e)–139.2(h), magnetic-field lines are shown as red curves, along with simulated proton fluence (blue) for direct comparison.

The simulations show similar formation and collision of magnetized ribbons, stagnation of the flows, and formation of an extended current sheet, which saturates at a width comparable to the ion skin depth. We find excellent agreement and reproduction of the formation of a caustic proton focusing feature on the back side of each ribbon. This feature is tracked in both experiment and simulation with excellent agreement and is shown in Fig. 139.3. The initial inflow speed, based on half the rate of change of the ribbon separation, is ~$1 \times 10^6$ m/s. The collision velocity decreases as the ribbons collide and eventually stagnates for $t > 3$ ns.

The reconnection in the simulation occurs in a very fast burst, yielding the magnetic islands already growing and visible in the simulations at 3.12 ns. Several profiles of the electric fields constituting different components of the generalized Ohm's law are shown in Fig. 139.4. The peak electric field in the simulations, near $1.5 \times 10^7$ V/m, is comparable to "fastest-possible" reconnection rates inferred from reconnection inflows $v_{\text{ribbon}} = 1 \times 10^6$ m/s and $B$ fields of the order of 25 T. Even accounting for flux pileup,[23] the simulated reconnection rates are extremely fast, close to 100% of the local Alfvénic rate $V_A^* B^*$, calculated based on the compressed magnetic fields and the plasma density in the current sheet. We find that the high compressibility of the current sheet, resulting from the supersonic inflows, drives this reconnection rate, which is significantly beyond what can be expected in steady-state reconnection.

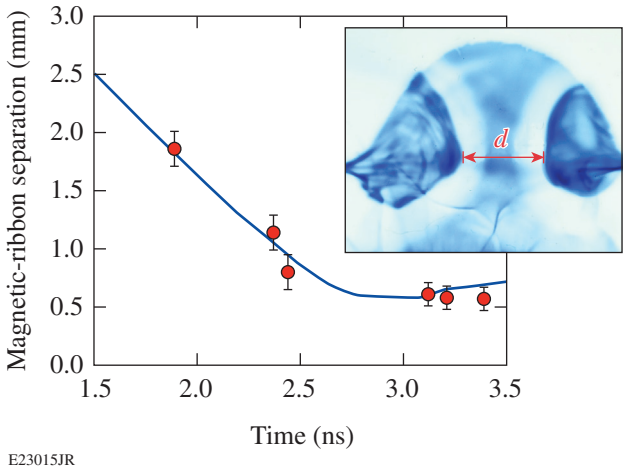


Figure 139.3
Measured time dependence of the separation $d$ between the outer caustic boundaries of the magnetic ribbons (data points) compared with particle-in-cell (PIC) simulations (curve) showing inflow and stagnation of the flows.

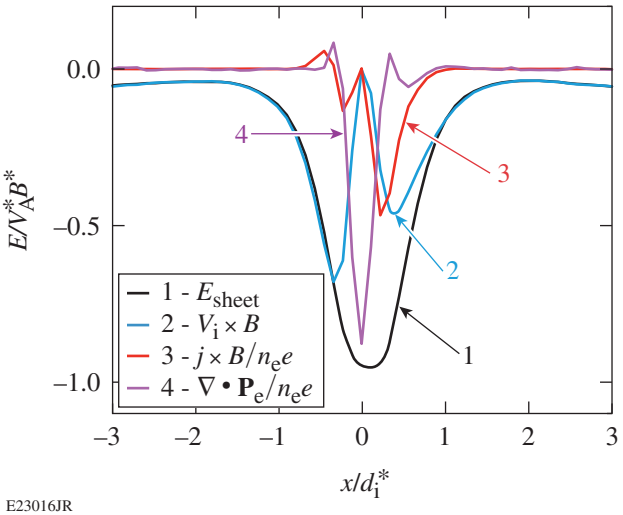


Figure 139.4
Generalized Ohm's law at the peak of reconnection. The (1) total electric field $E_{\text{sheet}}$ in the current sheet is compared to (2) the magnetohydrodynamic (MHD) field $V_i \times B$, (3) the Hall field $j \times B/n_e e$, and (4) the electron pressure tensor $\nabla \bullet \mathbf{P}_e / n_e e$. The electric fields are shown in units of $V_A^* B^*$, which are the maximum values of Alfvén speed and the magnetic field across the compressed current sheet. The ion skin depth is $d_i^*$.

The reconnection phase is followed by a complete magnetic annihilation, which is currently still in disagreement between experiment and simulation. In the simulated proton radiograph, the overall structure of the current sheet persists *after the reconnection* for some time. This is due to a confluence of factors, including a small but finite amount of unreconnected magnetic field upstream and an incomplete outflow of magnetic flux out of the current sheet, but primarily the persistence of the magnetic islands in the current sheet (which have nowhere to go). Despite reconnection and island formation, a finite magnetic field remains in the current sheet and continues to appear in the simulated radiographs. In contrast, by 3.39 ns

in the experimental data, there is a disruption of this current sheet structure, such that protons are no longer deflected at all. It is likely that three-dimensional (3-D) effects not captured in the simulations are important for the fast disruption. Magnetic islands are special structures in 2-D and could exhibit new dynamics in 3-D, allowing for the complete disruption of the sheet current.

In summary, the magnetic reconnection of externally magnetized, colliding plumes of HED plasma has been demonstrated for the first time. The experimental results and numerical simulations show the formation and collision of magnetic ribbons, the pile-up of the magnetic flux, and reconnection of the magnetic field. The reconnection is fast, with a reconnection rate comparable to the Alfvén reconnection rate. The experimental results are generally in very good agreement with first-principles PIC simulations that model the experiments from end to end. Some features of the experiment, however, like the fast annihilation of the current sheet after the reconnection, are not displayed by the 2-D simulations and will be investigated in full-scale, 3-D simulations.

## ACKNOWLEDGMENT

This work is supported by the U.S. Department of Energy under Contracts No. DE-NA0001944, DE-SC0007168, DE-SC0008655, and DE-SC0006670; the National Laser Users' Facility program; the University of Rochester; and the New York State Energy Research and Development Authority. The particle-in-cell simulations were conducted on the Jaguar and Titan supercomputers through the Innovative and Novel Computational Impact on Theory and Experiment (INCITE) program. This research used resources of the Oak Ridge Leadership Computing Facility located in the Oak Ridge National Laboratory, which is supported by the Office of Science of the U.S. Department of Energy under Contract No. DE-AC05-00OR22725.

## REFERENCES

1. E. R. Priest and T. Forbes, *Magnetic Reconnection: MHD Theory and Applications* (Cambridge University Press, Cambridge, England, 2000).
2. D. Biskamp, *Magnetic Reconnection in Plasmas*, Cambridge Monographs on Plasma Physics (Cambridge University Press, Cambridge, England, 2000).
3. M. Yamada, R. M. Kulsrud, and H. Ji, Rev. Mod. Phys. **82**, 603 (2010).
4. A. Bhattacharjee, Annu. Rev. Astron. Astrophys. **42**, 365 (2004).
5. M. Yamada *et al*., Phys. Plasmas **1**, 3269 (1994).
6. N. A. Crocker *et al*., Phys. Rev. Lett. **90**, 035003 (2003).
7. A. Bhattacharjee, Z. W. Ma, and X. Wang, Phys. Plasmas **8**, 1829 (2001).
8. B. V. Somov *et al*., Adv. Spacers Res. **32**, 1087 (2003).
9. M. Machida and R. Matsumoto, Astrophys. J. **585**, 429 (2003).
10. J. Goodman and D. Uzdensky, Astrophys. J. **688**, 555 (2008).
11. P. M. Nilson, L. Willingale, M. C. Kaluza, C. Kamperidis, S. Minardi, M. S. Wei, P. Fernandes, M. Notley, S. Bandyopadhyay, M. Sherlock, R. J. Kingham, M. Tatarakis, Z. Najmudin, W. Rozmus, R. G. Evans, M. G. Haines, A. E. Dangor, and K. Krushelnick, Phys. Rev. Lett. **97**, 255001 (2006).
12. C. K. Li, F. H. Séguin, J. A. Frenje, J. R. Rygg, R. D. Petrasso, R. P. J. Town, O. L. Landen, J. P. Knauer, and V. A. Smalyuk, Phys. Rev. Lett. **99**, 055001 (2007).
13. P. M. Nilson, L. Willingale, M. C. Kaluza, C. Kamperidis, S. Minardi, M. S. Wei, P. Fernandes, M. Noley, S. Bandyopadhyay, M. Sherlock, R. J. Kingham, M. Tatarakis, Z. Najmudin, W. Rozmus, R. G. Evans, M. G. Haines, A. E. Dangor, and K. Krushelnick, Phys. Plasmas **15**, 092701 (2008).
14. J. Zhong *et al*., Nat. Phys. **6**, 984 (2010).
15. Q.-L. Dong *et al*., Phys. Rev. Lett. **108**, 215001 (2012).
16. W. Fox, G. Fiksel, A. Bhattacharjee, P. Y. Chang, K. Germaschewski, S. X. Hu, and P. M. Nilson, Phys. Rev. Lett. **111**, 225002 (2013).
17. L. J. Waxer, D. N. Maywar, J. H. Kelly, T. J. Kessler, B. E. Kruschwitz, S. J. Loucks, R. L. McCrory, D. D. Meyerhofer, S. F. B. Morse, C. Stoeckl, and J. D. Zuegel, Opt. Photonics News **16**, 30 (2005).
18. O. V. Gotchev, J. P. Knauer, P. Y. Chang, N. W. Jang, M. J. Shoup III, D. D. Meyerhofer, and R. Betti, Rev. Sci. Instrum. **80**, 043504 (2009).
19. M. Borghesi *et al*., Plasma Phys. Control. Fusion **43**, A267 (2001).
20. M. Borghesi *et al*., Phys. Rev. Lett. **92**, 055003 (2004).
21. N. L. Kugland, J. S. Ross, P. Y. Chang, R. P. Drake, G. Fiksel, D. H. Froula, S. H. Glenzer, G. Gregori, M. Grosskopf, C. Huntington, M. Koenig, Y. Kuramitsu, C. Kuranz, M. C. Levy, E. Liang, D. Martinez, J. Meinecke, F. Miniati, T. Morita, A. Pelka, C. Plechaty, R. Presura, A. Ravasio, B. A. Remington, B. Reville, D. D. Ryutov, Y. Sakawa, A. Spitkovsky, H. Takabe, and H. S. Park, Phys. Plasmas **20**, 056313 (2013).
22. P. B. Radha, V. N. Goncharov, T. J. B. Collins, J. A. Delettrez, Y. Elbaz, V. Yu. Glebov, R. L. Keck, D. E. Keller, J. P. Knauer, J. A. Marozas, F. J. Marshall, P. W. McKenty, D. D. Meyerhofer, S. P. Regan, T. C. Sangster, D. Shvarts, S. Skupsky, Y. Srebro, R. P. J. Town, and C. Stoeckl, Phys. Plasmas **12**, 032702 (2005).
23. W. Fox, A. Bhattacharjee, and K. Germaschewski, Phys. Rev. Lett. **106**, 215003 (2011).
24. W. Fox, A. Bhattacharjee, and K. Germaschewski, Phys. Plasmas **19**, 056309 (2012).